Structural and Multidisciplinary Optimization (2025) 68:36
https://doi.org/10.1007/s00158-025-03962-8

RESEARCH PAPER

Connectivity-driven topology optimization for path-following compliant mechanism: a formulation with predictive volume constraints and adaptive strategies for gray element suppression

Lidan Zhang[1] · **Stijn Koppen**[1] · **Fred van Keulen**[1]

Received: 11 August 2024 / Revised: 3 December 2024 / Accepted: 30 December 2024

Abstract
We propose a topology optimization (TO) formulation and related optimization scheme for designing compliant mechanisms following a user-defined trajectory. To ensure the broad applicability and achieve precisely control of the outputs, geometric nonlinearity with incremental solutions are considered. A challenge in the design optimization of these structures is the development of formulations with satisfactory balance between (i) precise trajectory control and (ii) proper connectivity between the input/output ports and the support. Previously proposed density-based topology optimization formulations typically lack the promotion of the desired load-transferring connections, or usually complicate the design using mixed shape, size, and topology variables to enforce a minimum connectivity. To simplify design progress using exclusive topology variables, i.e., purely density-based TO methods, we propose a relatively straightforward formulation involving commonly used response functions, such as compliance and volume as constraints. For the constraints, the paper provides a scheme for defining corresponding upper limits. Numerical examples of challenging shell and plate design optimization problems demonstrate the effectiveness of the proposed formulation and scheme in the generation of load-transferring connections while limiting the impact on the performance of the path generation functionality.

Keywords Topology optimization · Path-following compliant mechanism · Connectivity · Geometric nonlinearity

1 Introduction

Density-based topology optimization (TO) was initially mostly applied in linear stiffness design (Bendsøe and Sigmund 1999; Buhl et al. 2000). Since then, the method is widely used for many other design purposes (Dirksen et al. 2012; Otomori et al. 2012; Lu et al. 2013; Wang et al. 2020). One of the prevalent applications is compliant mechanisms (Pedersen et al. 2001; Sigmund 1997; Bruns and Sigmund 2004), for which, Density-based TO allows creating highly complex and sophisticated structures that would be challenging to design based on intuition. A class of typically complicated-to-design compliant mechanisms is known as path generation compliant mechanisms (PGCMs). A PGCM's output ports can move following a user-defined trajectory, when, for example, displacements or forces are applied to the input ports. To achieve precise control of the output ports along the defined trajectory, nonlinear analysis with incremental solutions are prevalent adopted in topology optimization for PGCMs. Furthermore, even though practical applications may require linear relationships between inputs and outputs, the mechanism itself may exhibit finite deflections and rotations. Consequently, it is necessary to consider geometric nonlinearity in potential designs for ensuring broad applicability, for example decoupled $X-Y$ stages (Yong et al. 2008; Lai et al. 2012; Awtar and Parmar 2013) and linear guide actuators (Olfatnia et al. 2012; Huang et al. 2009; Weingrod et al. 2013).

To design PGCMs using Density-based TO, it could be challenging to automatically promote connectivity between input, output ports, and supporting boundaries. A typical result exhibiting lack of connectivity is shown in Fig. 1, where the objective is to minimize the squared in-plane displacements of the center point at multiple pseudo-time

Responsible editor: Shikui Chen

✉ Lidan Zhang
l.zhang-5@tudelft.nl

[1] Computational Design and Mechanics, Delft University of Technology, Mekelweg 2, 2628 CD Delft, The Netherlands

Published online: 24 February 2025

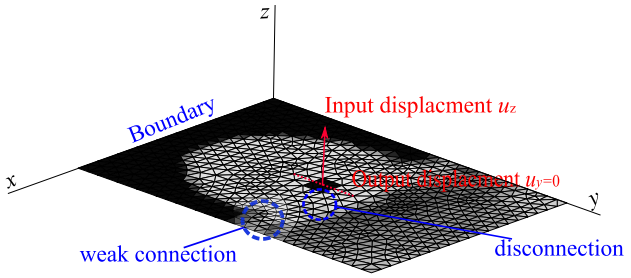

Fig. 1 A topology optimization result without connectivity. The objective is to minimize the squared in-plane displacements u_y of the center point at multiple pseudo-time points given a prescribed out-of-plane displacement u_z. Here, black represents solid material (pseudo-density ρ_e=1), white void ($\rho_e = 0$), and gray those in between ($0 < \rho_e < 1$). The middle black block represents a non-design area. The design shows both disconnections with void elements and weak connections with gray elements

points given a prescribed out-of-plane displacement. The optimizer opts here to converge to the obvious trivial solution of disconnecting the center point. Although this design can achieve the specified goal, it lacks physical meaning in the real world.

For the issue illustrated in Fig. 1, the reason, as stated in Pedersen et al. (2001), is the lack of force transfer requirements among the input, output, and the support in purely density-based TO methods. To ensure connectivity, two methodologies are generally employed: one involves incorporating force transfer requirements into the density-based TO, while the other abandon purely density-based TO, but proposing a different parameterization method, such as incorporating size and shape design variables. The latter approach has been extensively explored in previous works. First, shape variables can ensure the connectivity. Wang and Tai (2008) and Tai et al. (2002) expressed structural topology by mapping a set of Bezier curves onto a fixed finite element mesh, which connected input to output ports. Along the Bezier curves, materials were allowed to grow on the finite element mesh to form a new structural topology. Due to the inherent continuity of Bezier curves, any topology mapped from these curves always maintains connectivity. Lu and Kota (2005), as well as Zhou and Ting (2004) segment the load path into multiple sections, where the length and position of each section were then designed. This, in turn, guarantees the structural connectivity among the input and output ports. For the above method, it is necessary to determine an initial shape guess, which often requires some level of domain knowledge, engineering intuition, or prior experience. Furthermore, given that shape design variables are involved in the methods mentioned above, related sensitivity calculations become relatively difficult. Thus, zero-gradient methods, e.g., genetic algorithms (GA) are prevalent choices adopted in the mentioned works instead of more efficient gradient-based methods. Second, connectivity can be ensured by size variables corresponding to ground structures' elements. Saxena (2004), Rai et al. (2006a, b, 2007, 2009), Naik et al. (2010, 2011), and Nagendra Reddy et al. (2012), focusing on frame element-based ground structures, designed PGCM by adjusting, for example, the length and height of frame elements. Given that an intermediate value of such design variable is manufacturable, no connectivity issues as in purely density-based TO are encountered. However, the size control method may be restricted to ground structure-based designs and may not be easily applied to other types of elements, such as plates and shells, which can be manufactured more readily using laser cutting.

Another approach to enhance connectivity in path generation mechanisms is through the use of hexagonal-tessellated finite elements and negative masks design parameterization (Saxena 2008, 2011; Kumar and Saxena 2022). Briefly, they discrete the design domain by Hexagonal elements, then, utilizing movable masks to define the topology, where material inside the mask is removed. By utilizing edge-connected Hexagonal elements and the proposed boundary smoothing techniques (Kumar and Saxena 2015), they can form hinge-free designs. Besides, as is verified in their previous work, using masks with hexagonal elements helps ensure the minimum and maximum length scales in the topology, consequently obtaining readily manufacturable designs (Singh et al. 2020). However, ensuring length scales or changing the design parameterization may not address all kinds of connection issues, such as the case study for which the result is shown in Fig. 1. Here, the weak connections could be resolved, but the disconnections may not. Consequently, the hexagonal tessellation combined with negative mask method may also not solve the disconnections shown in Fig. 1. In previous work related to designs of contact-aided compliant mechanisms (Kumar et al. 2016, 2017, 2019, 2021), indeed, no disconnection issue like the one shown in Fig. 1 is encountered. This could be that the connectivity between their outputs/inputs and boundaries are implicitly indicated in complex path generation requirements. In our cases, we explore relatively simple paths focusing on specific timing positions. In this context, disconnections like those depicted in Fig. 1 may be more easily encountered. Furthermore, the hexagonal tessellation combined with negative mask method may not be readily applied to shells and plates, which are light-weighted, easily manufactured, and potentially exhibiting large deflections compared to its footprint.

To explore methods that are easily implemented and versatile for various elements and structures—especially shells and plates, which are easily manufactured using techniques like laser cutting—we will focus on density-based topology optimization (TO) methods. These methods are readily available, easy to apply to any type of element, and do not require domain knowledge for initial designs. When applying density-based TO, load transfer

requirement is a possibility for promoting the connectivity. For considering load transfer requirement for PGCM designs, several related work can be found. Saxena and Ananthasuresh (2001) introduced springs to output ports during the optimization procedure. The springs can avoid forming disconnections, but the required stiffness of the spring is difficult to decide. Pedersen et al. (2001) considered three load cases in the nonlinear analysis to ensure connectivity, which are: (1) without any force at the output port, (2) with a force at the output port aligned with the trajectory, and (3) with a force at the output port perpendicular to the trajectory. The design was mandated to follow the desired trajectory in all three load cases, which promotes the connectivity of a path generation design. Although the formulation is general and effective, the solution progress faces overwhelming computing efforts due to nonlinear matrix updating and refactorization. Furthermore, gray elements would still appear in the results. For the latter, Reinisch et al. (2021) introduced stress constraints to the method in Pedersen et al. (2001). However, stress constraints could further increase computational time. Moreover, optimization formulations that involve stress constraints may encounter issues with singular optima, necessitating additional treatments (Cheng and Guo 1997). Recognizing the intricacies of past methods, there is a compelling need to explore a streamlined, versatile, and effective approach. This aims to guarantee seamless connectivity and suppress undesired gray areas, paving the way for a more efficient and universally applicable design methodology.

To tackle the challenges mentioned above corresponding to density-based TO, we follow Koppen et al. (2022) and introduce a straightforward optimization formulation aimed at promoting connectivity, whose parameter selection scheme is illustrated to suppress the gray elements. The proposed formulation, which is introduced in Sect. 3, involves commonly used compliance and volume functions as constraints and, consequently, is easily extended to any structure and optimization algorithm. The upper limits of mentioned constraints are defined by the proposed embedded parameter selection strategy, which is explored extensively in Sect. 4. Next, several numerical examples in Sect. 5 verify the effectiveness of the proposed formulation and solution scheme. We use shells and plates in our numerical examples because of their slender nature and coupling between stretching and bending, which make them ideal for designing relatively large-displacement compliant mechanisms and promising for achieving complex path generation requirements. Moreover, many practical compliant mechanisms can be and are being manufactured from plates and thin-walled tubes, utilizing techniques, such as laser cutting.

2 Formulations

To achieve connectivity and potentially further suppress gray elements in the design of PGCMs, one typical option is to include appropriate constraints in the optimization formulations. In this section, our primary focus is on identifying suitable and easily implemented constraints through mathematical analysis of the corresponding optimization formulations. Prior to delving into the optimization formulation for PGCMs, we introduce fundamental concepts of a general density-based topology optimization formulation in Sect. 2.1. Here, the knowledge related to Lagrange multipliers and the reason of forming gray elements provide the basis for the proposed formulations in Sect. 2.2 and the optimization scheme in Sect. 3. Consequently, relatively elaborate introductions are given in this section.

2.1 Density-based topology optimization formulation

A topology density-based optimization problem can be generally expressed by

$$\min_{\boldsymbol{\rho}} \; f_0(\boldsymbol{\rho}), \tag{1}$$

$$\text{s.t. } g_l(\boldsymbol{\rho}) \le 0, \quad \forall l = \{1, \dots, q\} \quad , \tag{2}$$

$$\mathbf{0} < \boldsymbol{\rho}_0 \le \boldsymbol{\rho} \le \mathbf{1}. \tag{3}$$

Here, f_0 is an objective function, g_l is the l constraint, q is the number of constraints, $\boldsymbol{\rho}$ is the pseudo-density, $\boldsymbol{\rho}_0$ is the lower limit of $\boldsymbol{\rho}$, and $\mathbf{1}$ is the upper limit of $\boldsymbol{\rho}$ with all components equal to 1. Typically, to solve an optimization problem with inequality constraints, a Lagrange function involving f_0 and g_l is defined as

$$L(\boldsymbol{\rho}, y_l) = f_0(\boldsymbol{\rho}) + \sum_{l=1}^{q} y_l g_l(\boldsymbol{\rho}), \tag{4}$$

where $y_l \ge 0$ represents a Lagrange multiplier expressed by

$$y_l = \frac{\partial L}{\partial g_l}, \tag{5}$$

which reflects the relationship between the Lagrange function and the constraint during the optimization process. From Eq. (4), it follows that the constraints contribute to the Lagrange function only when $y_l > 0$. This knowledge is used in the following sections to select the upper limits of the constraints.

Moreover, if we express a constraint g_l by a variable term w_l combined with a constant term (the upper limit) $\overline{w}_l$, i.e., $g_l(\boldsymbol{\rho}) = w_l(\boldsymbol{\rho}) - \overline{w}_l$, the Lagrange multiplier y_l is then

$$y_l = -\frac{\partial L(\boldsymbol{\rho}, y_l, \overline{w}_l)}{\partial \overline{w}_l}. \tag{6}$$

Given the above, when optimization comes to a stationary point ($\boldsymbol{\rho}^*$,y_l^*), according to the envelope theory, (6) is transformed to

$$y_l^* = -\frac{\partial f_0(\boldsymbol{\rho}^*, \overline{w}_l)}{\partial \overline{w}_l}, \tag{7}$$

which defines the relationship between the objective value f_0 and the upper limit $\overline{w}_l$. From Eq. (7), by analyzing the Lagrange multiplier at the converged point, we can predict how changes in the upper limit will impact the objective value. This understanding is central to our optimization scheme outlined in Sect. 3, where users can adjust the constraint upper limits to suppress gray elements further, according to the desired objective error tolerance.

After introducing the Lagrange multipliers, the original optimization problem can be transformed to

$$\min_{\boldsymbol{\rho}_0 \le \boldsymbol{\rho} \le \mathbf{1}} \max_{y_l \ge 0} L(\boldsymbol{\rho}, y_l). \tag{8}$$

By exploring the minimizing problem related to $\boldsymbol{\rho}$ shown in Eq. 8, we can understand why there are gray elements, based on the partial derivative of L with respect to ρ_k:

$$\frac{\partial L}{\partial \rho_k} = \frac{\partial f_0}{\partial \rho_k} + \sum_{l=1}^{q} y_l \frac{\partial g_l}{\partial \rho_k}. \tag{9}$$

Here, if $\frac{\partial L}{\partial \rho_k} > 0$, reducing element k's density would reduce L. Consequently, in the next iteration, the design variable value of element k will lower. Conversely, if $\frac{\partial L}{\partial \rho_k} < 0$, in the next iteration, the element k's density will increase. When $\frac{\partial L}{\partial \rho_k} = 0$, there is no need for the optimizer to increase or reduce ρ_k, potentially resulting in an intermediate density value between the upper and lower limits, i.e., a gray element. The latter is usually alleviated by introducing black–white projection schemes, such as Heaviside filter. However, only by pushing elements to become black–white possibly results in topologies consisting of disjoint solid areas. One possibility to effectively enhance the connectivity in density-based TO is to carefully selected constraints for PGCM designs. Details about how the constraints are selected from a mathematical aspect is illustrated in the next section.

2.2 Formulations for designing path generation compliant mechanisms

In this section, we present a simple optimization formulation for establishing connectivity in path generation designs using density-based topology optimization (TO) methods. We first describe the objective function. Then, we propose two essential constraints and explain their importance for establishing the connectivity from a mathematical aspect.

To meet a path generation requirement when both shape and timing are important, usually, several precision points are used to represent an user-defined path followed by the mechanism. Each precision point is denoted by a pair of input and output values, i.e., ($u_{i,j}^{\text{in}}$, $u_{i,j}^{\text{out}}$) where j and i represent the indexes of precision points and degrees of freedom, respectively. The inputs here are closely tied to the incremental steps in the nonlinear analysis. For the outputs, in the desired (user-defined) path, they are predetermined. While in the realized path, it is calculated through nonlinear analysis. During the optimization process, efforts are made to minimize the disparity between the desired path and the realized path. Consequently, the object function is expressed by

$$f_0 = \sum_{i=1}^{n} \sum_{j=1}^{m} \alpha_{i,j} \left(u_{i,j}^{\text{out}} - u_{i,j}^{*} \right)^2. \tag{10}$$

Here, $u_{i,j}^{\text{out}}$ and $u_{i,j}^{*}$ denote the outputs on the realized and desired paths, receptively. Besides, m represents the number of precision points, n is the number of degrees of freedom (DOFs), and $\alpha_{i,j}$ represents a weight factor. The latter is set to 1 in the work but can be adjusted if different precision points have different levels of importance.

If we take the above objective function and conduct an unconstrained optimization, the Lagrange function is the objective function itself. Then, the gradient of the Lagrange function, i.e., the objective function f_0, with respect to ρ_k can be expressed by

$$\frac{\partial f_0}{\partial \rho_k} = \sum_{i=1}^{n} \sum_{j=1}^{m} 2\alpha_{i,j} \left(u_{i,j}^{\text{out}} - u_{i,j}^{*} \right) \frac{\partial u_{i,j}}{\partial \rho_k}. \tag{11}$$

When the unconstrained optimization problem reaches the optimum, it satisfies the condition $\frac{\partial f_0}{\partial \rho_k} = 0$. As defined in Sect. 2.1, $\frac{\partial f_0}{\partial \rho_k} = 0$ would lead to gray elements. Hence, it is highly probable that the connectivity is not established.

In order to establish connectivity, we consider constraints that can contribute non-zero sensitivities. Usually, a mechanism following user-defined paths is desired to maintain sufficient stiffness to support a load in its undeformed configuration, i.e., within the linear scope. For the latter, information can usually be found in stiffness specifications of a design. It defines the load a mechanism must carry in

its undeformed configuration and the allowed displacement given the load. By utilizing the information, we can set a linear compliance constraint expressed by

$$g_c = C_s - \overline{C}_s \quad \forall s = \{1, \dots, q\}. \tag{12}$$

Here, C_s is the compliance calculated in a separate linear load case with a load $(\mathbf{F}_L)_s$ applied in s-direction, q is the number of directions where compliance constraints are required, and $\overline{C}_s$ is the corresponding upper limit defined by the user, which can be determined as $(\mathbf{F}_L \overline{\mathbf{u}}_L)_s$. Here, $(\overline{\mathbf{u}}_L)_s$ is the allowable displacement given this load.

Next, for simplification, we assume that only one compliance constraint is involved. Then, the Lagrange function can be expressed by

$$L = f_0 + y_c(C - \overline{C}), \tag{13}$$

where y_c denotes the multiplier for the compliance constraint. The gradient of L with regard to ρ_k is

$$\frac{\partial L}{\partial \rho_k} = \frac{\partial f_0}{\partial \rho_k} + y_c \frac{\partial C}{\partial \rho_k}. \tag{14}$$

If $\frac{\partial f_0}{\partial \rho_k}$ approaches 0, $\frac{\partial L}{\partial \rho_k}$ depends on $y_c \frac{\partial C}{\partial \rho_k}$. In this situation, regarding $y_c > 0$, if $y_c \frac{\partial C}{\partial \rho_k} < 0$ and not close to 0, then $\frac{\partial L}{\partial \rho_k} < 0$ and the pseudo-density of element k will increase. If $y_c \frac{\partial C}{\partial \rho_k}$ is close to 0, then $\frac{\partial C}{\partial \rho_k}$ is close to 0, which means the element k currently has almost no influence on both the objective and the compliance constraints. In other words, element k contributes to nothing but increase the volume. In this case, the element could be gray and floating in the design domain, which is defined as a useless element. To remove such an element, a volume constraint $g_v = V - \overline{V}$ can be introduced to the optimization formulation, where V presents the design's volume and $\overline{V}$ the corresponding upper limit. With the volume constraint, the Lagrange formulation can be expressed by

$$L = f_0 + y_c(C - \overline{C}) + y_v(V - \overline{V}), \tag{15}$$

where y_v denotes the multiplier for the volume constraint. The gradient of L with regard to an element pseudo-density ρ_k is

$$\frac{\partial L}{\partial \rho_k} = \frac{\partial f_0}{\partial \rho_k} + y_c \frac{\partial C}{\partial \rho_k} + y_v \frac{\partial V}{\partial \rho_k}. \tag{16}$$

Here, we only discuss the situation when $y_v > 0$ and $y_c > 0$. If both $\frac{\partial f_0}{\partial \rho_k}$ and $\frac{\partial C}{\partial \rho_k}$ are near to zero, $\frac{\partial L}{\partial \rho_k}$ is completely dependent on the value of $y_v \frac{\partial V}{\partial \rho_k}$. Since the sensitivity of the volume constraint $\frac{\partial V}{\partial \rho_k}$ is always positive, we have $\frac{\partial L}{\partial \rho_k} > 0$ indicating that the element will be removed and the issue related to useless elements (materials) is resolved. The only chance for (16) to render an intermediate element density is when $y_c \frac{\partial C}{\partial \rho_k} = -y_v \frac{\partial V}{\partial \rho_k}$, but this rarely happens in practice. If it happens, we can still disrupt the balance by adjusting the upper limits. Since stiffness is often specified as a design requirement, in this study we choose to adjust the upper limit of the volume constraint. By introducing the compliance and volume constraints, the proposed formulations can be finally summarized as

$$\begin{aligned} &\min_{\boldsymbol{\rho}} f_0(\boldsymbol{\rho}) = \sum_{i=1}^{n} \sum_{j=1}^{m} \alpha_{i,j} (u_{i,j}^{\text{out}}(\boldsymbol{\rho}) - u_{i,j}^{*})^2, \\ &\text{s.t. } C_s(\boldsymbol{\rho}) < \overline{C}_s, \quad \forall s = 1, \dots, q \\ &V < \overline{V}, \\ &\mathbf{0} < \boldsymbol{\rho}_0 \le \boldsymbol{\rho} \le \mathbf{1}. \end{aligned} \tag{17}$$

According to the discussions above, we still have several questions to answer: (1) How we can ensure both $y_v > 0$ and $y_c > 0$? (2) How we can define the initial upper limits of volume constraints? (3) When and how we can adjust the volume upper limits? These questions are important for promoting connectivity and suppressing gray elements. So in the next section, we will answer these questions by proposing a parameter selection scheme which is embedded in the optimization progress.

3 Optimization scheme for path generating mechanisms

In this section, we propose an optimization scheme, involving the prediction and adjustment of $\overline{V}$ to obtain connectivity and suppressing gray elements for PGCM designs. A general scheme is shown in Fig. 2 and explanations are followed.

- **Predictive progress**. Initially, the upper limit of the volume constraint can be roughly estimated by aggregating the volume of beneficial elements at several optimization steps, where these elements exhibit negative objective sensitivities with respect to their pseudo densities, as described in Sect. 2.1. The prediction becomes more accurate when considering optimization steps with a positive compliance constraint Lagrange multiplier $y_c > 0$, as only then does the compliance constraint contribute to the objective and connectivity (see Sect. 2.2). Based on these considerations, we perform predictive optimization for 20 iterations, which is typically sufficient for a relatively accurate estimation. During the optimization, with compliance constraints (but not the volume constraint yet), we aggregate the volume of beneficial elements at each step where $y_c > 0$, and the average of

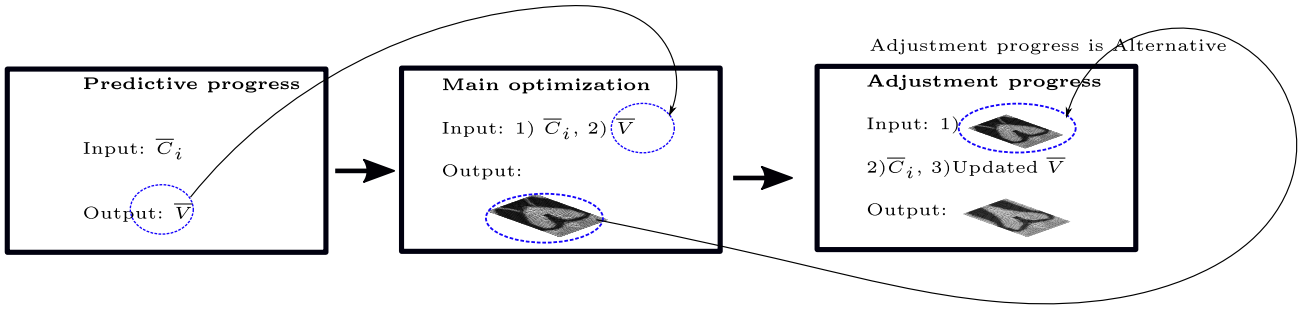

Fig. 2 A general three-progress optimization scheme to ensure a clear topology. Firstly, a known upper limit of compliance $\overline{C}_i$ is used to predict the upper limit of volume $\overline{V}$. With the predicted $\overline{V}$, the optimization starts with both volume and compliance constraints, and we call this progress Main optimization. From the Main optimization, a topology with promoted connectivity will be obtained. Then, alternatively, we can further suppress the gray element by conducting an adjustment progress, where the converged topology from the Main optimization will be taken as the start point, and volume will be adjusted according to objective error allowance. The adjustment progress is alternative, the user can also consider using suitable post-processing method to deal with remained gray elements. But please notice that post-processing method could influence the performance of manufacturing prototypes

these values across all steps is taken as the upper limit of the volume constraint $\overline{V}$. If y_c remains zero throughout the prediction, the smallest recorded value is used. A pseudo-algorithm for this prediction process is shown in Algorithm 1.

- **Main optimization**. After the predictive progress, we obtain the volume upper limit. Then with both the volume and compliance constraints, we can conduct the main optimization progress. Here, we suggest to start the main optimization from scratch instead of from the end of the predictive progress. Since in the topology of the latter, clusters of solid elements surrounded by void elements, referred to as "islands," can appear. The "islands" can eventually be removed with a latter applied volume constraint, but may require more optimization iterations than expected and could result in a sub-optimal local minimum. After convergence of the main optimization, the connectivity between input/output points and supporting boundaries can be promoted. Alternatively, we can proceed with the adjustment process to further suppress gray elements.
- **Adjustment progress**. In the adjustment progress, we start from the converged topology in the main optimization progress and continue with a reduced $\overline{V}$. A decrease of $\overline{V}$ is usually followed by an increase of the objective value, that is, the squared error of paths. Thus, the decrease of $\overline{V}$ should be determined based on the error tolerance specified in the design requirements. The error tolerance is related to how much performance the designer is willing to lose to make the product manufacturable. Allowing more error increases the chances of suppressing gray elements. Then, according to the error tolerance, we can define the change of $\overline{V}$ using (7). However, if the reduction in $\overline{V}$ is relatively substantial, the prediction by (7) may not be accurate since (7) is verified for a small region around the optimal point. To address this issue, we can readjust $\overline{V}$ after the optimization achieves a new equilibrium and continue the optimization with the new $\overline{V}$. The adjustment strategy is outlined in Algorithm 2, which takes the converged topology from Main optimization as the start point. After each volume adjustment, the optimization just continue instead of restarting from the beginning. The adjustment progress is optional. Users can also use post-processing methods to handle gray elements. However, post-processing methods might affect the performance of manufacturing prototypes, and the extent of this influence is unpredictable.

Algorithm 1 Prediction progress for defining the upper limit of the volume constraint $\overline{V}$ with a known compliance value $\overline{C}$. Here, i represents the optimization step, k is the element index, and $\frac{\partial f_0}{\partial \rho_k}$ is the sensitivity of the objective function w.r.t. the pseudo-density of element k. According to our experience, $\beta_0 = 20$ iterations are enough for an initial guess of the volume upper limit.

$\beta_0 \leftarrow 20$ ▷ *Number of iterations in the prediction progress
$\gamma \leftarrow 0$ ▷ *Number of optimization steps where $y_c > 0$
$V_{\text{total}} \leftarrow 0$ ▷ *Sum of volume
$V_{\min} \leftarrow 10^5$ ▷ *Minimum of volume
for i $= \{1, ..., \beta_0\}$ **do**
  Conduct optimization step i with $\overline{C}$, then
  for k $= \{1, ...,$ number of elements$\}$ **do**
    if $\frac{\partial f_0}{\partial \rho_k} < 0$ **then**
      $V_i \leftarrow V_i + V_k$
    end if
  end for
  if $y_c > 0$ **then**
    $V_{\text{total}} \leftarrow V_{\text{total}} + V_i$
    $\gamma \leftarrow \gamma + 1$
  end if
  if $V_{\min} > V_i$ **then**
    $V_{\min} \leftarrow V_i$
  end if
end for
if $\gamma > 0$ **then**
  $\overline{V} \leftarrow \frac{V_{\text{total}}}{\gamma}$
else
  $\overline{V} \leftarrow V_{\min}$
end if

Algorithm 2 Adjustment progress. The progress is optional and conducted after the convergence of the main optimization progress, only if gray elements appear in the convergence topology. Here, f_0 represents the convergence objective value at the end of the main optimization progress, y_{v} is the corresponding Lagrange multiplier at the end of the main optimization progress, f_0^{new} is the objective value at the new stationary point after an adjustment of $\overline{V}$, and $y_{\text{v}}^{\text{new}}$ is the corresponding Lagrange multiplier at the new stationary point. We set a threshold 0.1, if the difference between the expected and achieved objective is smaller than 0.1, we stop the progress.

Require: Δf_0 ▷ *Allowable increase of objective if $\overline{V}$ is decreased
$f^{\text{expected}} \leftarrow f_0 + \Delta f_0$ ▷ *Expected objective after volume adjustment
$\Delta\overline{V} \leftarrow \Delta f_0 / y_{\text{v}}$
$\overline{V} \leftarrow \overline{V} - \Delta\overline{V}$
Next, continue optimization with $\overline{C}$ and $\overline{V}$, starting from the converged topology of Main optimization to a new convergence, then
$y_{\text{v}} \leftarrow y_{\text{v}}^{\text{new}}$
$\Delta f_0 \leftarrow f^{\text{expected}} - f^{\text{new}}$
while Abs$(\frac{\Delta f_0}{f^{\text{expected}}}) > 0.1$ **do**
  $\Delta\overline{V} \leftarrow \Delta f_0 / y_{\text{v}}$
  $\overline{V} \leftarrow \overline{V} - \Delta\overline{V}$
  Next, continue optimization with $\overline{C}$ and $\overline{V}$ to a new convergence, then
  $y_{\text{v}} \leftarrow y_{\text{v}}^{\text{new}}$
  $\Delta f_0 \leftarrow f^{\text{expected}} - f^{\text{new}}$
end while

4 Numerical examples

Four examples are given in this section to illustrate the effectiveness of the proposed formulation and solution scheme with the first two concerning plates and the last two shells. In the first example, we test the ability of the volume constraint to remove useless elements. For the second plate example, we explore how the objective value changes when the volume upper limits change. Then, in the third example, we demonstrate the ability of the formulation to design a mechanism exhibiting a complex path. Finally, we design a structure that has input and output ports in different locations. In the following examples, SIMP method (Bendsøe and Sigmund 1999) is used to generate the topology, which is typically solved by MMA method. Displacements required in SIMP are calculated by incremental-iterative methods (De Borst et al. 2012), where only geometric nonlinearity is taken into account. 6-Nodes–12-DOF shell elements are employed (Van Keulen and Booij 1996). The method we proposed can be combined with any type of elements. We utilize irregular mesh is simple due to it is readily available in our code. Furthermore, using irregular meshes could be benefit irregular design domain and boundary conditions in future work if needed. The optimization criteria in the following is (1) the relative change of the objective value smaller than 0.01 for continuous 50 optimization steps and (2) reach the maximum number of optimization iterations, which is 1000.

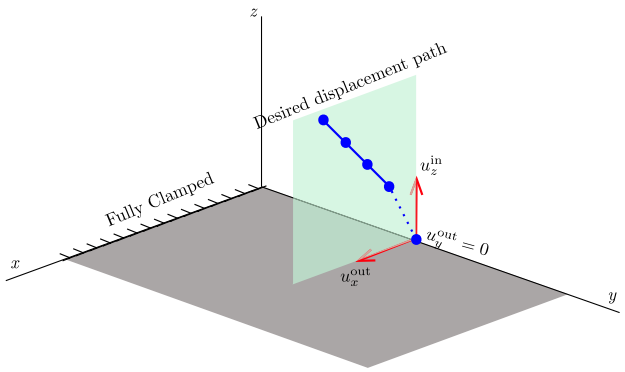

$x \times y \times z$	$20 \times 30 \times 1$mm
$u^{\text{in}}_{z,j}$	$8, 12, 16, 20$mm
$(u^*_{x,j}, u^*_{y,j})$	$(2,0), (4,0), (6,0), (8,0)$mm
E	300GPa

Fig. 3 A cantilever plate model. The blue line, which has four precision points, represents the required displacement path. A part of the path is indicated by a dashed line since we are not concerned with moving from the beginning position to the first precision point. The red arrows represent the local coordinate system in which the locations of precision points are defined. Poisson's ratio is 0.3. (Color figure online)

4.1 A plate-based compliant mechanism tracing a slant line

The first illustration shows how a plate mechanism is developed. The cantilever plate in Fig. 3 serves as the design domain. The right sides' center node is intended to follow the user-defined path indicated by the blue line. Displacements in the x and y directions are outputs involved in the objective function, whereas displacements in the z-direction are prescribed as inputs. The related optimization parameters are listed in Table 1.

The optimization results are displayed in Table 2. Here, (a) shows the result ignoring the compliance constraint where the connectivity to the supporting boundary is not promoted. Whereas, a clear topology is obtained in (b) by incorporating both compliance and volume restrictions. Here, since no disconnected structures and gray areas appear, the adjustment step is not required. In (c), we only include the compliance constraint but exclude the volume. Here, the result contains more solid material than the one in (b), but the extra material is meaningless since they hardly affect the objective value. Furthermore, the extra material is eliminated from (c) by including the volume constraint.

Table 1 The specification of constraints' upper bounds for the slant line–tracing plate mechanism design

Symbols	Values	Comments
F_z^{L}	0.01 N	Prescribed
u_z^{L}	0.25×10^{-3} cm	Prescribed
$\overline{C}$	2.5×10^{-6} N cm	$F_z^{\text{L}} \times u_z^{\text{L}}$
$\overline{r_{\text{v}}}$	0.57	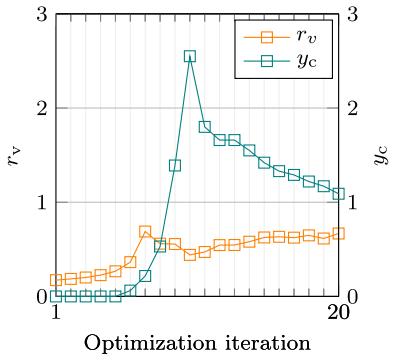
$\overline{V}$	$0.57V_{\text{t}}$	$\overline{r_{\text{v}}} \times V_{\text{t}}$

The upper limit for compliance constraint $\overline{C}$ is set by specific stiffness requirements, specifically by the prescribed load F_z^{L} and allowable maximum displacement u_z^{L}. The upper limit for volume constraint $\overline{V}$ is defined by the prediction progress shown in Algorithm 1 with 20 optimization iterations. For each iteration, in the figure of the 5th row, we record the Lagrange multiplier for the compliance constraint y_{c} and the volume percentage r_{v}. The later represents the volume of the beneficial elements w.r.t. that of the design domain V_{t}. The average value of r_{v} is given in the row. Finally, $\overline{V}$ is calculated in the last row

Table 2 Topology results of the plate mechanism tracing a slant line

Index	Topology	$\overline{C}$ (N cm)	$\overline{V}$	f_0 (cm × cm)	$\mu^{\text{obj}}_{\text{error}}$ (%)
(a)	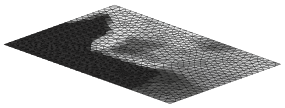	None	$0.57V_t$	1.02×10^{-5}	0.16
(b)	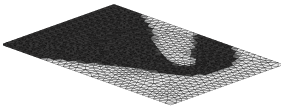	2.5×10^{-6}	$0.57V_t$	9.90×10^{-3}	4.97
(c)	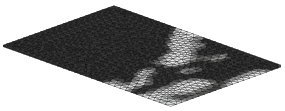	2.5×10^{-6}	None	9.82×10^{-3}	4.95
(d)	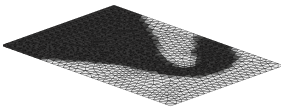	2.5×10^{-6}	$0.57V_t$	9.91×10^{-3}	4.97

(a) Acts as a comparison, illustrating the connectivity issue in the density-based TO if the proposed method is not applied. (b) The output of main optimization starting from the scratch. (c) Shows the results without volume constraints starting from the scratch. (d) Shows the ability of volume constrains to remove extra elements starting from (c). Here, f_0 represents the real objective value and $\overline{C}$ and $\overline{V}$ are the upper limits for compliance and volume constraints, respectively, whose definition is shown in Table 1. The relative objective error is then defined as $\mu^{\text{obj}}_{\text{error}} = \frac{\sqrt{f_0}}{|u_{\max}|}$, where $u_{\max} = 2$cm presents the maximum displacement

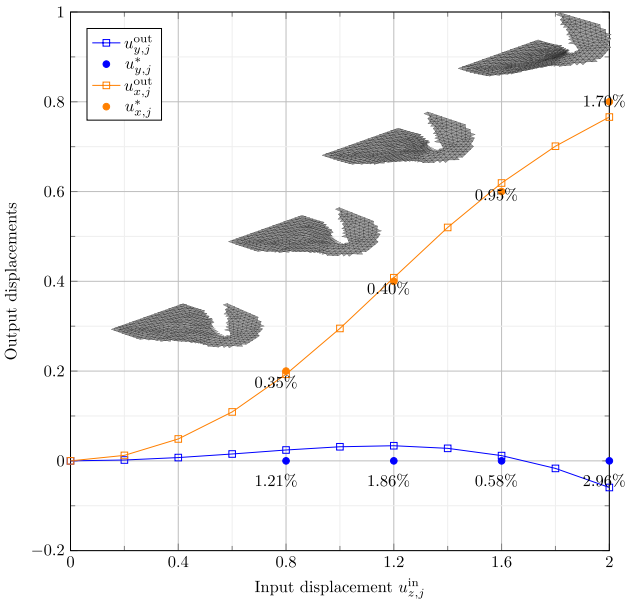

Fig. 4 Deformation curves and deformed configurations for the topology shown in (a) of Table 2, the latter which are coupled to four precision points. The percentage values denotes the relative displacement error $\mu^{\text{d}}_{\text{error}} = \frac{|u^{\text{out}}_{i,j} - u^*_{i,j}|}{|u_{\max}|}$

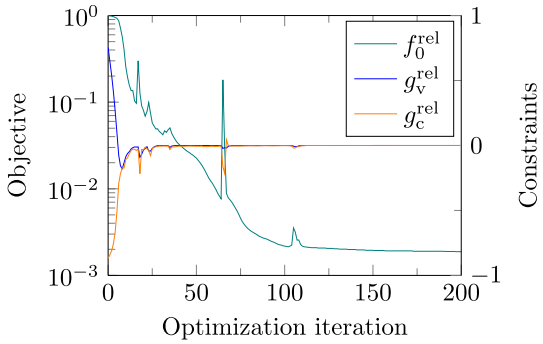

Fig. 5 Optimization convergence of the slant line–tracing plate mechanism. The objective shown here, is the value relative to that of the initial solid design. For the compliance constraint, which is relative to the upper limit, i.e., $g_{\text{c}}^{\text{rel}} = \frac{g_{\text{c}}}{\overline{C}}$. For the volume constraint, which is relative to that of the design domain, i.e., $g_{\text{v}}^{\text{rel}} = \frac{g_{\text{v}}}{V_{\text{t}}}$. The upper limits of volume and compliance constraints are constant as depicted in Table 1

Starting optimization with (c) and include the volume constraint, we can get the result (d), which is nearly the same as (a). The transition from (c) to (d) also illustrates the volume constraint's ability to eliminate unnecessary material.

The deformed configurations and deflection curves for the results displayed in (b) of Table 2 are presented in Fig. 4.

It is shown that the design is able to trace the user-defined path with relative small errors. The result demonstrates that rather than attempting to zero out all displacement errors, minimizing the objective can be accomplished by balancing positive and negative displacements.

The optimization iteration history is shown in Fig. 5. Oscillations are typically observed in the early stages, and peaks often appear when the compliance restriction is close to be activated, where an increase in objective is accompanied by a decrease in compliance. In other words, here

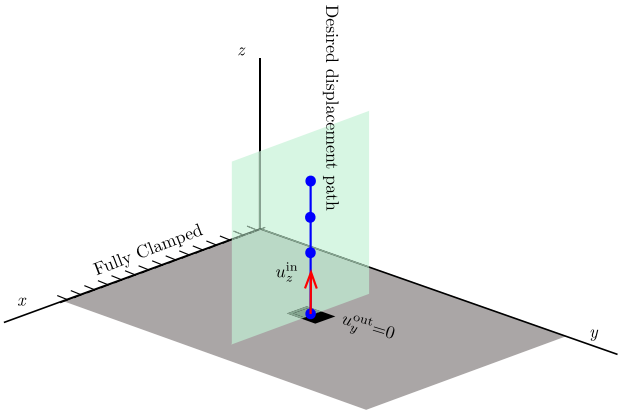

$x \times y \times z$	$20 \times 30 \times 0.8$mm
$u_{z,j}^{\text{in}}$	$10, 15, 20$mm
$u_{y,j}^{*}$	$0, 0, 0$mm
E	300GPa

Fig. 6 A plate model tracing a normal line. The desired displacement path is shown by the blue line, which is approximated by three precision points. A one-dimension local coordinate system shown by the red arrows is used to describe the points. Poisson's ratio is 0.3. (Color figure online)

Table 3 The specification of constraints' upper bounds for the plate mechanism tracing a normal line

Symbols	Values	Comments
F_z^{L}	0.01 N	Prescribed
u_z^{L}	0.4×10^{-3} cm	Prescribed
$\overline{C} = F_z^{\text{L}} \times u_z^{\text{L}}$	4×10^{-6} N cm	
$\overline{r_{\text{v}}}$	0.45	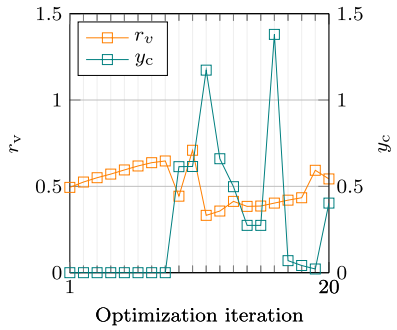
$\overline{V}$	$0.45V_{\text{t}}$	$\overline{r_{\text{v}}} \times V_{\text{t}}$

Here, $\overline{C}$ is set by specific stiffness requirements. The upper limit for volume constraint $\overline{V}$ is defined by the prediction progress shown in Algorithm 1 with 20 optimization iterations. For each iteration, in the figure of the 5th row, we record the Lagrange multiplier for the compliance constraint y_{c} and the volume percentage r_{v}. The later represents the volume of the beneficial elements w.r.t. that of the design domain V_{t}. The average value of r_{v} is given in the row. Finally, $\overline{V}$ is calculated in the last row

optimization strikes a balance between two different intermediate designs, one that reduces objective and the other that reduce the compliance, i.e., increasing stiffness. After 150 optimization iterations, oscillations vanish, and after 200 iterations, the optimization reaches a convergence.

4.2 A plate-based compliant mechanism tracing a normal line

This example produces a trajectory mechanism from the cantilever plate seen in Fig. 6. The middle black block indicates a non-design domain. The structural central node is meant to follow the displacement path indicated by the blue line. As input, the displacement in the z-direction is specified. The displacement along the y-axis is considered as the output. To define the upper limit $\overline{C}$, we load the structure by F_z^{L} at the structural central node in a separate linear load case. Assuming the allowable maximum displacement u_z^{L} is prescribed, we can obtain $\overline{C}$. Next, with $\overline{C}$, we define $\overline{V}$. All the aforementioned parameters are listed in Table 3.

Topology results are depicted in Table 4. As illustrated in row (a), if the compliance constraint is ignored, we fail to generate the connection to the supporting boundary. If both compliance and volume constraints are applied, the connectivity is developed and shown in the (b). However, the design might be enhanced since gray areas are visible along the supported side. Therefore, the adjustment step is required for suppressing the gray elements. We allow a relative objective function error $\left(\mu_{\text{error}}^{\text{obj}} = \frac{\sqrt{f_0}}{|u_{\text{max}}|}\right)$ up to 6.5%. The upper limit of the volume constraint is then modified according to Algorithm 2 and a better topology is ultimately produced shown in (c). The corresponding deformed configurations and deflection paths are illustrated in Fig. 7. It is observable that the structural central point can trace the normal line with displacement errors $\mu_{\text{error}}^{\text{d}}$ of less than 6%.

The convergence history in Fig. 8 provides information on how the volume upper limit $\overline{V}$ varies during the whole optimization. As seen in Fig. 8a, $\overline{V}$ remains constant in the main optimization progress and equal to the value specified in Table 3. The optimization converge around 200 iterations. Then, the adjustment progress is shown in Fig. 8b, where the new $\overline{V} = 0.34V_{\text{t}}$ is set by (7), which involves the objective error 6.5% and the volume constraint's current Lagrange multiplier y_{v}. Starting with the new volume upper limit after another 100 iterations, the objective converges to a value larger than the predicted one shown by the dashed line. This is because (7) only works in a small region near the convergence point. With $\Delta\overline{V}$ getting larger, the objective values at new convergence points gradually deviate from the predicted

Table 4 Topology results of the plate mechanism tracing a normal line

Index	Topology	$\overline{C}$ (N cm)	$\overline{V}$	f_0 (cm × cm)	$\mu_{\text{error}}^{\text{obj}}$ (%)
(a)	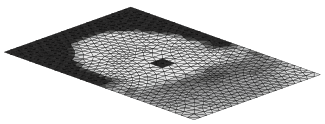	None	$0.45V_t$	3.11×10^{-6}	0.09
(b)	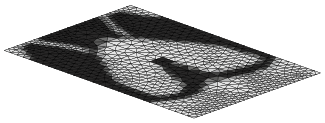	4×10^{-6}	$0.45V_t$	5.88×10^{-3}	3.83
(c)	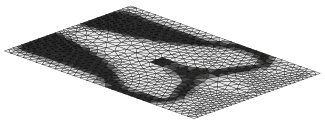	4×10^{-6}	$0.37V_t$	1.71×10^{-2}	6.54

(a) Acts as a comparison, illustrating the connectivity issue in the density-based TO if the proposed method is not applied. The result is not an output from our proposed scheme. (b) The output of main optimization starting from the scratch. (c) The output of adjustment progress starting from (b). Here, $\overline{C}$ and $\overline{V}$ are upper limits for compliance and volume constraints. For $\overline{V}$, specifically, $0.45V_t$ is from the predictive progress (Algorithm 1) and $0.37V_t$ is the upper limit at the end of the adjustment progress (Algorithm 2). f_0 is the real objective value. $\mu_{\text{error}}^{\text{obj}} = \frac{\sqrt{f_0}}{|u_{\max}|}$ denotes the relative objective error where $u_{\max}$ presents the maximum displacement

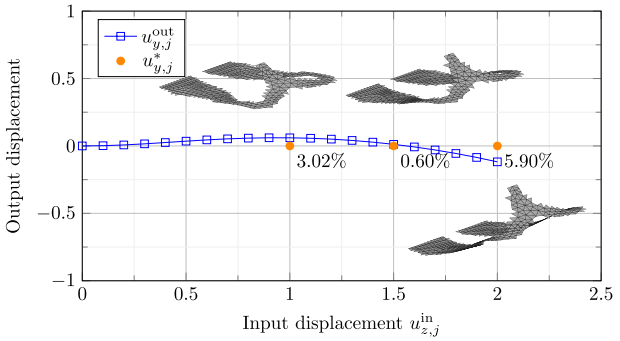

Fig. 7 Deformation curves and deformed configurations for the topology shown in (c) of Table 4. The percentage values denotes the relative displacement error $\mu_{\text{error}}^{\text{d}} = \frac{|u_{i,j}^{\text{out}} - u_{i,j}^{*}|}{|u_{\max}|}$

value calculated by (7) (see Fig. 9). To attain the predicted objective, we can adjust $\overline{V}$ again. According to the new converged y_v and the difference between current f_0 and the target f_0, the volume upper limit is then adjusted to $0.37V_t$. The above adjustment is consistent with the Algorithm 2. As seen in Fig. 8b, $\overline{V}$ is modified at 150 iteration and the objective converges to the predicted value after another 100 iterations.

4.3 A cylinder moving back and forth

This example presents a shell mechanism, with its design domain 70% of a cylinder surface shown in Fig. 10. The structure bottom is fully clamped. The center node of the top side is designed to move along the displacement path shown by the blue line. The displacement in z-direction is prescribed as the input. The displacement along the x-direction is regarded as the output. In this case, we constrain both the stiffness along x and y directions. So two separate linear load cases are applied. In one load case, the structure is loaded by F_x^{L} and in the other, is loaded by F_z^{L} at the top center node. According to allowable u_x^{L} and u_z^{L}, upper limits of compliance constraints are calculated. Next, $\overline{V}$ is defined by the predictive optimization progress. The mentioned parameters are shown in Table 5

Topology results are detailed in Table 6. Involving both compliance and volume constraints, the topology result is shown in (a). Although the connectivity is established, the design is preferable to be improved since gray areas are visible. We assume that $\mu_{\text{error}}^{\text{obj}}$ can be increased by 5%. Then, a clear final topology is shown in row (b). The relevant deformation configurations and curves can be found in Fig. 11. It is seen that the final design can achieve the desired behavior, i.e., moving back and forth with a displacement error $\mu_{\text{error}}^{\text{d}} < 10\%$.

The convergence history in Fig. 12 provides information on how the volume upper limit $\overline{V}$ varies during the whole optimization progress. Figure 12a shows the progress from scratch to the converged design shown in (a) of Table 6. Here, $\overline{V}$ maintains the value defined in Table 5 as a constant. Although oscillations are encountered due to constraint violation, the objective and constraint values become relatively stable after 250 iteration steps and converge at 300 iteration. Then, starting from the converged design, $\overline{V}$ is reduced based on the allowable objective error and current Lagrange multiplier. After another 100

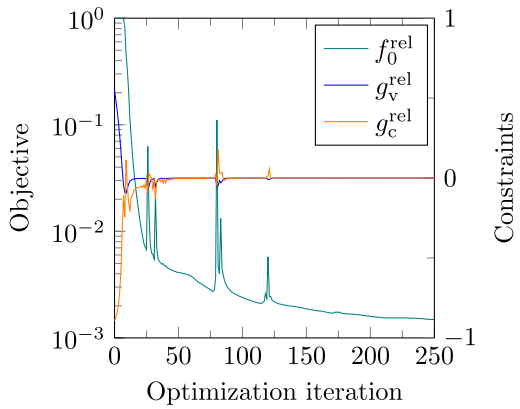

(a) Main optimization progress

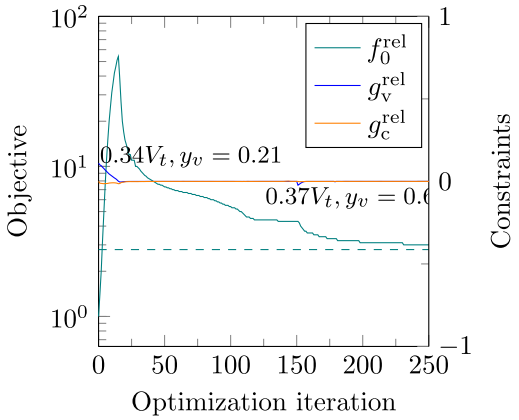

(b) Adjustement progress

Fig. 8 Convergence curve for the plate-based compliant mechanism tracing a normal line. **a** Main optimization progress. Optimization starting from the initial solid design with $\overline{C}$ and $\overline{V}$ defined in Table 3. The objective value is relative to the initial solid design. **b** Adjustment optimization progress starting from the converged design in **a**. The objective value is relative to the converged design in **a**. The dashed line shows the predicted objective. From 0 to 150 iterations, $\overline{V} = 0.34V_{\text{t}}$ where V_{t} is the volume of the design domain. From 150 to 250 iterations, $\overline{V} = 0.37V_{\text{t}}$. Here, V_{t} is the volume of the fully solid design. For the calculation of the volume upper limit, details can be seen in Algorithm 2

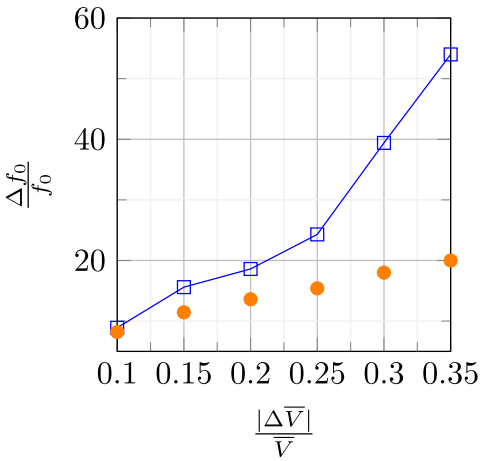

Fig. 9 Predicted (orange) and actual (blue) relative objective change $\frac{\Delta f_0}{f_0}$ as a function of $\frac{|\Delta \overline{V}|}{\overline{V}}$. The start point of this step is the design shown in (b) of Table 4 where $f_0 = 5.88 \times 10^{-3}$, $\overline{V} = 0.45V_{\text{t}}$, and $y_{\text{v}} = 0.21$. Predicted values are derived using (7), and actual values are obtained from optimization. (Color figure online)

iterations, optimization converges to a value larger than the prediction indicated by the dashed line. Then, $\overline{V}$ is adjusted based on the new y_{v}, and after another 50 iterations, the objective value finally converges to the predicted value. The aforementioned adjustment is consistent with Algorithm 2.

4.4 A gripper structure

This example depicts a gripper shell mechanism with independent input and output point locations. The design is derived from a half-cylinder surface shown in Fig. 13, which is fully clamped on the right side. The input point is the center node of the structure, and the output points are the structural upper and lower left corners. The output points are designed to move through the blue line. A half-cylinder surface is taken as the design domain due to symmetry. To involve the compliance constraint, we load the top left corner by F_x^{L} in a separate linear load case. Then, the upper limit $\overline{C}$ is calculated assuming that the allowable maximum displacement u_x^{L} is prescribed. Then $\overline{V}$ is defined by the predictive progress. The parameters mentioned above are shown in Table 7. Then, the optimization restarts with defined $\overline{V}$ and $\overline{C}$, finally a connected topology obtained in Fig. 14, and no adjustment progress is needed.

The corresponding deformed configurations and the deflection curves are presented in Fig. 15. It is seen that the mechanism follows the prescribed path well with relative displacement errors $\mu_{\text{error}}^{\text{d}} < 3\%$. The history of optimization iterations is shown in Fig. 16. It is seen that oscillation occurs for balancing between reducing compliance and minimizing the objective. Then after 300 iterations, the curves become stable and gradually converge.

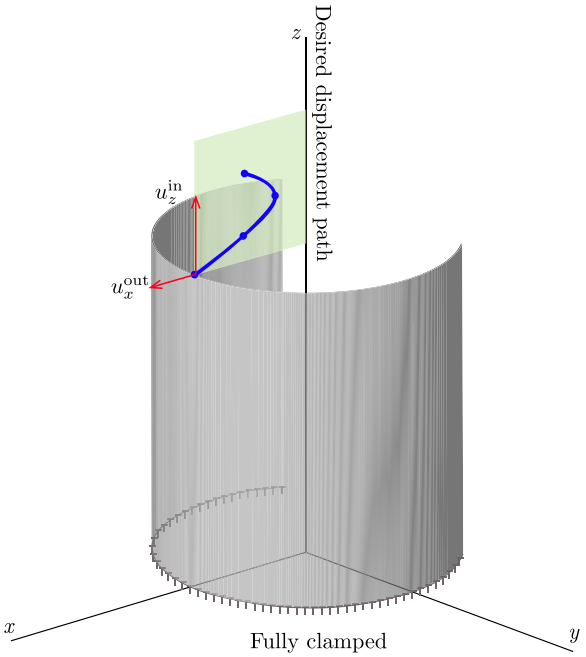

Radius × Height × Thickness	50 × 200 × 3mm
$u_{z,j}^{\text{in}}$	$10, 20, 40$mm
$u_{x,j}^{*}$	$-20, -40, -20$mm
E	100MPa

Fig. 10 A cylinder shell fully clamped at the bottom. The desired displacement of the output point is shown by the blue line. The path is approximated by three precision points. The positions of these points are described in the local coordinate system defined by the red arrows. Poisson's ratio is 0.3. (Color figure online)

Table 5 The specification of constraints' upper bounds for the shell mechanism moving back and forth

Symbols	Values	Comments
F_x^{L}	1 N	Prescribed
u_x^{L}	0.5 cm	Prescribed
$\overline{C}_x$	0.5 N cm	$F_x^{\text{L}} \times u_x^{\text{L}}$
F_z^{L}	1 N	Prescribed
u_z^{L}	0.15 cm	Prescribed
$\overline{C}$	0.15 N cm	$F_z^{\text{L}} \times u_z^{\text{L}}$
$r_{\text{v}}^{\min}$	0.3	
$\overline{V}$	$0.3V_{\text{t}}$	$r_{\text{c}}^{\min} \times V_{\text{t}}$

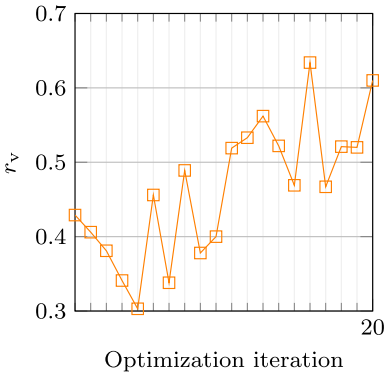

Here, $\overline{C}$ is set by specific stiffness requirements. $\overline{V}$ is defined by the prediction progress shown in Algorithm 1 with 20 optimization iterations shown in the figure. Here, only r_{v} is depicted since $y_{\text{c}} = 0$. Thus, the minimum r_{v} is used for calculating $\overline{V}$

Table 6 Topology results of the shell mechanism moving back and forth

Index	Topology	$\overline{C}$ (N cm)	$\overline{V}$	f_0 (cm × cm)	$\mu^{\text{obj}}_{\text{error}}$ (%)
(a)	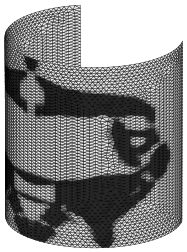	$\overline{C}_x = 0.5, \overline{C}_y = 0.15$	$0.3V_t$	0.0645	6.4
(b)	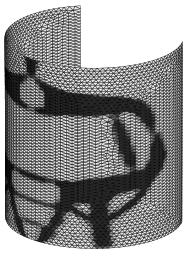	$\overline{C}_x = 0.5, \overline{C}_y = 0.15$	$0.236V_t$	0.2201	11.7

(a) The output of main optimization starting from the scratch. (b)The output of adjustment progress starting from (a). Here, $\overline{C}$ and $\overline{V}$ are upper limits for compliance and volume constraints. For $\overline{V}$, specifically, $0.3V_t$ is from the predictive progress (Algorithm 1), and $0.236V_t$ is the upper limit at the end of the adjustment progress (Algorithm 2). f_0 is the real objective. $\mu^{\text{obj}}_{\text{error}} = \frac{\sqrt{f_0}}{|u_{\max}|}$ denotes the relative objective error where $u_{\max}$ presents the maximum displacement

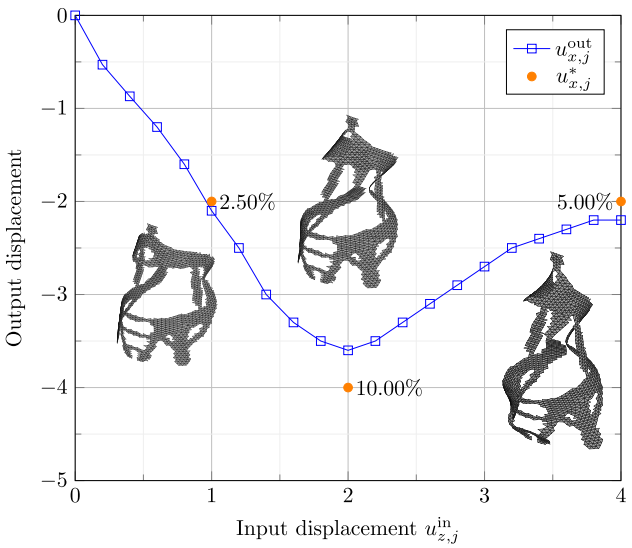

Fig. 11 Deformation curves and configurations for the topology shown in the first row of Table 6. Here, the deformation figures are coupled to three precision points. The percentage values denotes the relative displacement error $\mu^{\text{d}}_{\text{error}} = \frac{|u^{\text{out}}_{i,j} - u^{*}_{i,j}|}{|u_{\max}|}$

5 Conclusion

A formulation involving commonly used volume and compliance constraints are proposed to establish the connectivity among input, output, and if necessary fixture supporting the mechanism. An optimization scheme including (1) predictive step for defining the upper limits of volume, (2) main optimization step, and (3) adjustment step for further suppressing gray elements is proposed.

Numerical examples show that with the volume upper limit defined in the predictive step, a connectivity is typically promoted in the topology after the main optimization step. If gray elements appear, we can further suppress them by reducing the volume's upper limit. The influence of reducing volume upper limits on objective errors can be predicted by the value of Lagrange multipliers. The prediction is only effective within a small range around the optimum points. If the change is beyond the scope, one can adjust the upper limits again after optimization reaching a new stationary point.

In addition, instead of applying the adjustment step proposed in the optimization scheme, one can combine robustness presented in Wang et al. (2011) with our proposed formulations in the main optimization progress to ensure a gray element free design. However, given gray elements may not appear at the convergence of the main optimization step, both robust formulation and the adjustment step are not necessary.

Given the fact that stiffness of the structure is usually prescribed, the proposed method only considers adjusting volume upper limits to improve the obtained topology. If

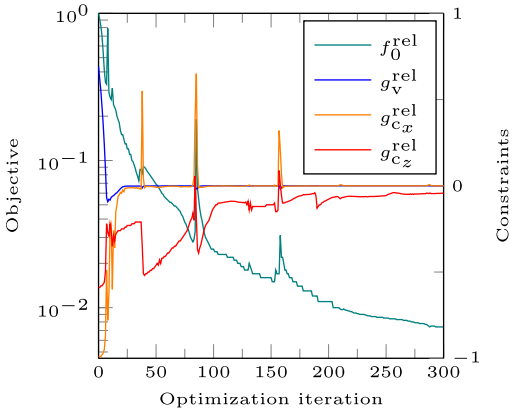

(a) Main optimization progress

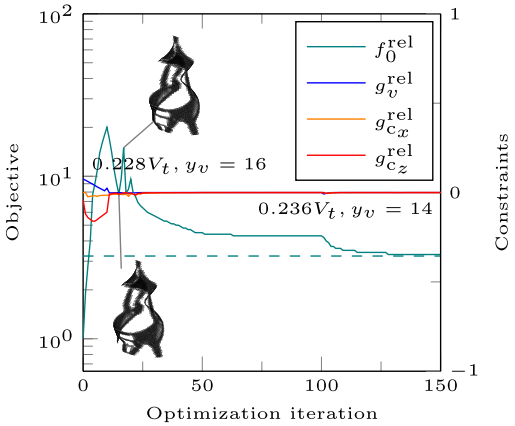

(b) Adjustment optimization progress

Fig. 12 Optimization progress for the shell mechanism moving back and forth. $g_{\text{c}_z}^{\text{rel}}$ presents compliance constraint relative to $\overline{C}_z$ and $g_{\text{c}_x}^{\text{rel}}$ that to $\overline{C}_x$. **a** Optimization starting from the fully solid design with $\overline{C}$ and $\overline{V}$ defined in 5. The objective value is relative to the initial solid design. **b** Adjustment optimization begins from the final design in **a**, with the objective value relative to that of the final design. The dashed line indicates the predicted objective value. In **b**, from 0 to 100 iteration, $\overline{V} = 0.228V_{\text{t}}$. From 100 to 150 iteration, $\overline{V} = 0.236V_{\text{t}}$. Here, V_{t} is the volume of the fully solid design. For calculation of the upper limits, details can be seen in Algorithm 2

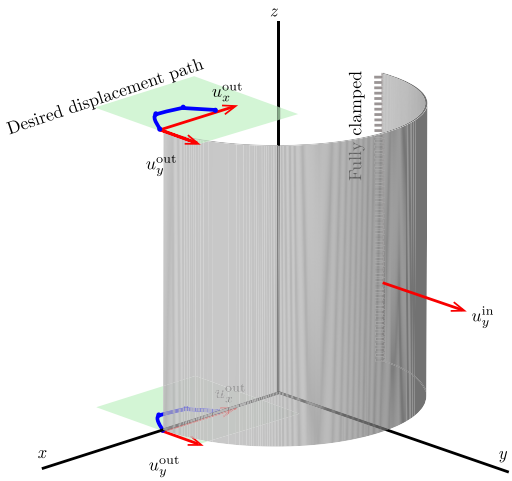

Radius × Height × Thickness	50 × 200 × 3mm
$u_{y,j}^{\text{in}}$	10, 16, 20mm
$(u_{x,j}^*, u_{y,j}^*)$	$(-5,-1.5),(-8,-1),(-10,0.01)$mm
E	1000MPa

Fig. 13 A cylinder shell fully clamped at the right side. The desired displacement of the output point is shown by the blue line. The path is approximated by three precision points. The positions of these points are described in the local coordinate system defined by the red arrows. Poisson's ratio is 0.3. (Color figure online)

Table 7 The specification of constraints' upper bounds for the gripper-like shell mechanism

Symbols	Values	Comments
F_x^{L}	1 N	Prescribed
u_x^{L}	0.05 cm	Prescribed
$\overline{C}_x$	0.05 N cm	$F_z^{\text{L}} \times u_z^{\text{L}}$
$\overline{r}_{\text{v}}$	0.628	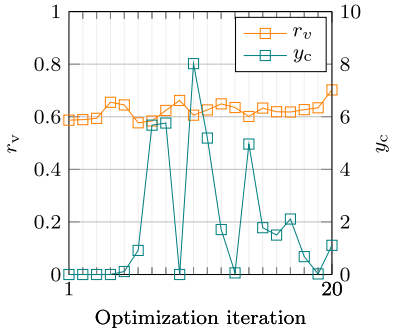
$\overline{V}$	$0.628V_{\text{t}}$	$r_{\text{v}} \times V_{\text{t}}$

Here, $\overline{C}$ is set by specific stiffness requirements. $\overline{V}$ is defined by the prediction progress (Algorithm 1) with 20 optimization iterations shown in the figure, where y_{c} and the ratio r_{v} is depicted. The average value of r_{v} for $y_{\text{c}} > 0$ is used to define $\overline{V}$

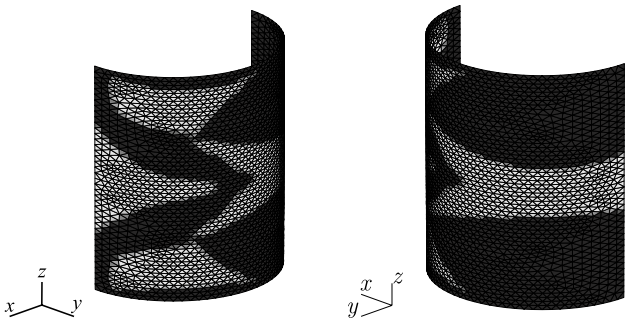

Fig. 14 Topology optimization result of the gripper mechanism. Objective value $f_0 = 9.38 \times 10^{-3}$ and relative objective error $\mu_{\text{error}}^{\text{obj}} = 4.8\%$

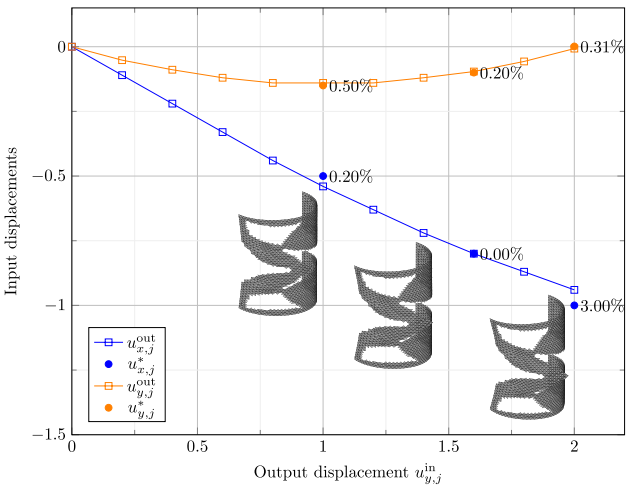

Fig. 15 Deformation curves and deformed configurations. The percentage values denotes the relative displacement error $\mu_{\text{error}}^{\text{d}} = \frac{|u_{i,j}^{\text{out}} - u_{i,j}^{*}|}{|u_{\max}|}$

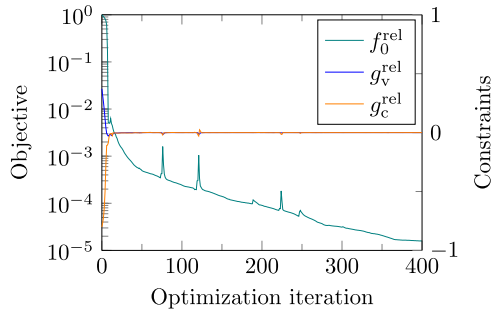

Fig. 16 Optimization convergence curve of the gripper shell mechanism. Objective f_0^{rel} is relative to the initial solid design. Here, the upper limits of volume and compliance constraints are consistent with those depicted in Table 7

stiffness is also allowed to change, then adjusting upper limits of compliance or even both constraints can also take effect.

Author contributions All authors contributed to the study conception and design. Material preparation, data collection, and analysis were performed by Lidan Zhang. The first draft of the manuscript was written by Lidan Zhang and all authors commented on previous versions of the manuscript. All authors read and approved the final manuscript.

Funding The work is supported by China Scholarship Council.

Data availability The input parameters and the output data have been included in the paper.

Declarations

Conflict of interest On behalf of all authors, the corresponding author states that there is no conflict of interest.

Replication of results The work is based on self-developed software named CHARLES, which was developed by Fred van Keulen for researching purposes in 1992. CHARLES is Pascal based and can only be run on the virtual machine where it was developed. Please contact Fred van Keulen or Lidan Zhang for the code, the virtual machine, and the tutorial for using CHARLES.

References

Awtar S, Parmar G (2013) Design of a large range xy nanopositioning system. J Mech Robot 5:021008

Bendsøe MP, Sigmund O (1999) Material interpolation schemes in topology optimization. Arch Appl Mech 69:635–654

Bruns T, Sigmund O (2004) Toward the topology design of mechanisms that exhibit snap-through behavior. Comput Methods Appl Mech Eng 193:3973–4000

Buhl T, Pedersen CB, Sigmund O (2000) Stiffness design of geometrically nonlinear structures using topology optimization. Struct Multidisc Optim 19:93–104

Cheng GD, Guo X (1997) ε-Relaxed approach in structural topology optimization. Struct Optim 13:258–266

De Borst R, Crisfield MA, Remmers JJ, Verhoosel CV (2012) Nonlinear finite element analysis of solids and structures. Wiley, Hoboken

Dirksen F, Berg T, Lammering R, Zohdi TI (2012) Topology synthesis of large-displacement compliant mechanisms with specific output motion paths. PAMM 12:801–804

Huang S, Tan KK, Lee TH (2009) Adaptive sliding-mode control of piezoelectric actuators. IEEE Trans Ind Electron 56:3514–3522

Koppen S, Langelaar M, van Keulen F (2022) A simple and versatile topology optimization formulation for flexure synthesis. Mech Mach Theory 172:104743

Kumar P, Saxena A (2015) On topology optimization with embedded boundary resolution and smoothing. Struct Multidisc Optim 52:1135–1159

Kumar P, Saxena A (2022) An improved material mask overlay strategy for the desired discreteness of pressure-loaded optimized topologies. Struct Multidisc Optim 65:304

Kumar P, Sauer RA, Saxena A (2016) Synthesis of c_0 path-generating contact-aided compliant mechanisms using the material mask overlay method. J Mech Des 138:062301

Kumar P, Saxena A, Sauer RA (2017) Implementation of self contact in path generating compliant mechanisms. In: Microactuators and micromechanisms: proceedings of MAMM-2016, Ilmenau, Germany, 5–7 Oct 2016. Springer, pp 251–261

Kumar P, Saxena A, Sauer RA (2019) Computational synthesis of large deformation compliant mechanisms undergoing self and mutual contact. J Mech Des 141:012302

Kumar P, Sauer RA, Saxena A (2021) On topology optimization of large deformation contact-aided shape morphing compliant mechanisms. Mech Mach Theory 156:104135

Lai L-J, Gu G-Y, Zhu L-M (2012) Design and control of a decoupled two degree of freedom translational parallel micro-positioning stage. Rev Sci Instrum 83:045105

Lu K-J, Kota S (2005) Topology and dimensional synthesis of compliant mechanisms using discrete optimization. J Mech Des 128:1080–1091. https://doi.org/10.1115/1.2216729

Lu L, Yamamoto T, Otomori M, Yamada T, Izui K, Nishiwaki S (2013) Topology optimization of an acoustic metamaterial with negative bulk modulus using local resonance. Finite Elem Anal Des 72:1–12

Nagendra Reddy BVS, Naik SV, Saxena A (2012) Systematic synthesis of large displacement contact-aided monolithic compliant mechanisms. J Mech Des 134:011007. https://doi.org/10.1115/1.4005326

Naik SV, Saxena A, Rai AK (2010) On the criteria for choice of the best solution from a generated set of partially compliant linkages. In: International design engineering technical conferences and computers and information in engineering conference, 2010, vol 44106, pp 685–694

Naik SV, Saxena A, Rai AK, Reddy BVSN (2011) How to choose from a synthesized set of path-generating mechanisms. J Mech Des 133:091009. https://doi.org/10.1115/1.4004608

Olfatnia M, Sood S, Gorman JJ, Awtar S (2012) Large stroke electrostatic comb-drive actuators enabled by a novel flexure mechanism. J Microelectromech Syst 22:483–494

Otomori M, Yamada T, Izui K, Nishiwaki S, Andkjær J (2012) A topology optimization method based on the level set method for the design of negative permeability dielectric metamaterials. Comput Methods Appl Mech Eng 237:192–211

Pedersen CB, Buhl T, Sigmund O (2001) Topology synthesis of large-displacement compliant mechanisms. Int J Numer Methods Eng 50:2683–2705

Rai AK, Saxena A (2007) Optimal continuum synthesis of partially compliant mechanisms for prescribed non-smooth paths. In: 13th National conference on mechanisms and machines (NaCoMM07), 2007. https://api.semanticscholar.org/CorpusID:56006954

Rai AK, Saxena A, Mankame ND (2006a) Synthesis of path generating compliant mechanisms using initially curved frame elements. J Mech Des 129:1056–1063. https://doi.org/10.1115/1.2757191

Rai A, Saxena A, Mankame ND, Upadhyay CS (2006b) On optimal design of compliant mechanisms for specified nonlinear path using curved frame elements and genetic algorithm. In: International design engineering technical conferences and computers and information in engineering conference, 2006, vol 42568, pp 91–100

Rai AK, Saxena A, Mankame ND (2009) Unified synthesis of compact planar path-generating linkages with rigid and deformable members. In: International design engineering technical conferences and computers and information in engineering conference, 2009, vol 49040, pp 223–232

Reinisch J, Wehrle E, Achleitner J (2021) Multiresolution topology optimization of large-deformation path-generation compliant mechanisms with stress constraints. Appl Sci 11:2479

Saxena A (2004) Synthesis of compliant mechanisms for path generation using genetic algorithm. J Mech Des 127:745–752. https://doi.org/10.1115/1.1899178

Saxena A (2008) A material-mask overlay strategy for continuum topology optimization of compliant mechanisms using honeycomb discretization. J Mech Des 130:082304. https://doi.org/10.1115/1.2936891

Saxena A (2011) Topology design with negative masks using gradient search. Struct Multidisc Optim 44:629–649

Saxena A, Ananthasuresh G (2001) Topology synthesis of compliant mechanisms for nonlinear force-deflection and curved path specifications. J Mech Des 123:33–42

Sigmund O (1997) On the design of compliant mechanisms using topology optimization. J Struct Mech 25:493–524

Singh N, Kumar P, Saxena A (2020) On topology optimization with elliptical masks and honeycomb tessellation with explicit length scale constraints. Struct Multidisc Optim 62:1227–1251

Tai K, Cui GY, Ray T (2002) Design synthesis of path generating compliant mechanisms by evolutionary optimization of topology and shape. J Mech Des 124:492–500

Van Keulen F, Booij J (1996) Refined consistent formulation of a curved triangular finite rotation shell element. Int J Numer Methods Eng 39:2803–2820

Wang NF, Tai K (2008) Design of grip-and-move manipulators using symmetric path generating compliant mechanisms. J Mech Des 130:112305. https://doi.org/10.1115/1.2976790

Wang F, Lazarov BS, Sigmund O (2011) On projection methods, convergence and robust formulations in topology optimization. Struct Multidisc Optim 43:767–784

Wang W, Munro D, Wang CC, van Keulen F, Wu J (2020) Space–time topology optimization for additive manufacturing. Struct Multidisc Optim 61:1–18

Weingrod I, Chou CY, Holmes B, Hom C, Irwin JW, Lindstrom O, Lopez F, Stubbs DM, Wüelser J-P (2013) Design of bipod flexure mounts for the IRIS spectrometer. In: Hatheway AE (ed) Optomechanical engineering 2013, SPIE, 2013, vol 8836. International Society for Optics and Photonics, pp 202–210. https://doi.org/10.1117/12.2024478

Yong YK, Aphale SS, Moheimani SR (2008) Design, identification, and control of a flexure-based xy stage for fast nanoscale positioning. IEEE Trans Nanotechnol 8:46–54

Zhou H, Ting K-L (2004) Topological synthesis of compliant mechanisms using spanning tree theory. J Mech Des 127:753–759. https://doi.org/10.1115/1.1900148